THE JOURNAL OF PHYSICAL CHEMISTRY LETTERS
A JOURNAL OF THE AMERICAN CHEMICAL SOCIETY

pubs.acs.org/JPCL Letter

# Laser-Accelerated Mass Transport in Oxygen Reduction Via a Graphene-Supported Silver–Iron Oxide Heterojunction

Joey Andrew A. Valinton, Min-Chuan Chung, and Chun-Hu Chen*

Cite This: *J. Phys. Chem. Lett.* 2022, 13, 4200–4206 Read Online

ACCESS | Metrics & More | Article Recommendations | Supporting Information

**ABSTRACT:** Mass-transport acceleration is essential toward enhanced electrocatalytic performance yet rarely recognized under irradiation, because light is usually reported to improve charge transfer. We studied laser-enhanced mass transport through the heterojunction between Ag and semiconductor $Fe_2O_3$ situated on graphene for oxygen reduction reaction. Because of the decreased mass-transport resistance by 59% under 405 nm laser irradiation, the current density can be enhanced by 180%, which is also supported by a theoretical calculation. This laser-enhanced mass transport was attributed to local photothermal heating and the near-field local enhancement. Easier desorption of $OH^-$ species occurring between the Fe and Ag centers under the laser accelerates the mass-transport centers.

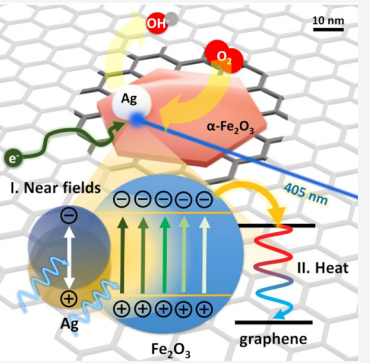




Increasing demands in renewable energy conversion require more efficient electrocatalysts. Highly efficient electrocatalysis requires the reactions to improve not only the charge transfer but also the mass transport of chemical species to and from the active sites. Recent electrocatalyst development focuses on overcoming the overpotential scaling relations and charge-transfer processes,[1] neglecting the role of mass transport. Although high surface-area approaches are commonly used to increase the yield of a reaction, sufficient mass transport is still required to achieve the goal of enhanced reactivity.[2] Thus, improving mass transport in electrocatalysis is important, yet design considerations are still lacking at present.

Light to enhance performance has been extensively reported in various types of electrocatalysis. In an oxygen reduction reaction (ORR), noble metal electrocatalysts (Pt, Pd, Au, and the alloys, etc.) have shown improved activities under white light (continuous wavelength) through a hot electron mechanism, as the result of surface plasmonic resonance.[3,4] A typical feature of the hot electron mechanism is decreasing the ORR onset bias under light,[3,5] corresponding to improving the charge transfer[6−9] instead of the mass transport. In the presence of other light-enhancement mechanisms,[10−12] there might be an overlooked possibility to accelerate mass transport by utilizing light to improve ORR electrocatalytic performance.

Harnessing the combination of light excitation between plasmonic metal and semiconductor could induce polarization to generate gradient differences. Because the heterojunction interface is the electrocatalytic active sites,[13−15] simultaneous surface plasmon and band gap excitation under light may elevate the ORR reactivity via accelerated mass transport. Although light-enhanced metal–semiconductor electrocatalysts have been present, many highlighted the plasmonic properties over the possible contributions of semiconductor excitations.[16−18] To investigate the origins and degrees of gradient differences, single-wavelength irradiation at the heterojunction becomes advantageous to prevent multiple, unrecognized excitations, thereby facilitating the identification of the possible wavelength-dependent features and/or other activity-contributing factors. With this, the dual excitation with a monochromatic laser at the interfaces is therefore a suitable strategy to study such mass-transport characteristic behaviors.

In this work, we reported a new phenomenon of laser-enhanced mass transport (LEMT) in ORR with a $Ag/Fe_2O_3$ heterojunction supported on N-doped graphene (Ag/FNG). Under static conditions, the 405 nm laser irradiation results in a significant decrease of mass transport resistance ($R_{mt}$) by 59% and a 180% increase of current density, while the charge-transfer resistance remains nearly identical. Electrochemical impedance spectroscopy (EIS) results confirm LEMT acting equivalent to electrode rotation. These unique behaviors cannot be completely explained by the widely recognized charge-transfer effect in the literature. Our studies discover a tandem mechanism of near-field enhancement and photothermal effect that both significantly accelerate mass transport. The transition from octahedral ($FeO_6$) to tetrahedral ($FeO_4$)

**Received:** March 10, 2022
**Accepted:** April 19, 2022
**Published:** May 5, 2022

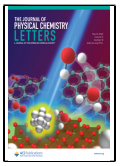





https://doi.org/10.1021/acs.jpclett.2c00709
*J. Phys. Chem. Lett.* 2022, 13, 4200–4206

species, when pairing up with Ag under a laser, enables the more rapid $OH^-$ desorption to accelerate mass transport than the dark conditions. This work reveals the possibility of achieving a remote, site-specific irradiation to elevate local ORR performance.

The synthesis of Ag/FNG was afforded by a two-step process (Figure 1a).[14] Iron(II) acetate was introduced to graphene oxide (GO) through refluxing under dimethylformamide to perform iron-assisted N-doping on graphene and eventual hybridization with hematite $Fe_2O_3$ upon a subsequent solvothermal treatment.[19] To effectively create the Ag/$Fe_2O_3$ heterojunction, silver nitrate ($AgNO_3$) was added on the reflux product before being subjected to a solvothermal treatment.

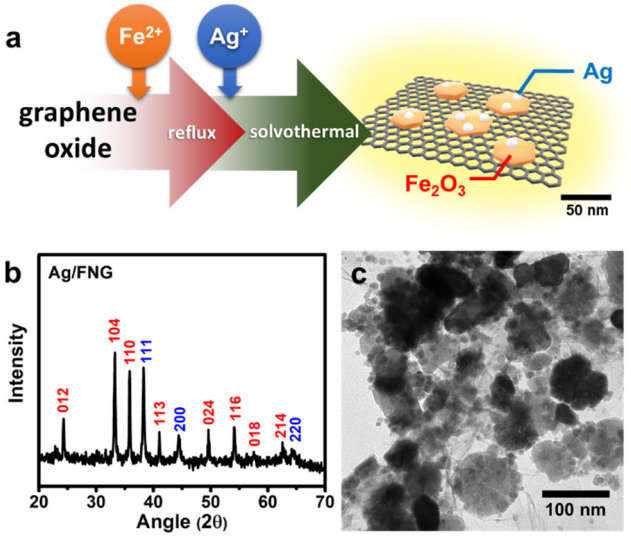


**Figure 1.** Synthesis of silver−iron oxide heterojunction on N-doped graphene oxide (Ag/FNG). (a) Scheme showing the sequential, two-step addition necessary to establish a Ag/$Fe_2O_3$ heterojunction in Ag/FNG. (b) XRD patterns of Ag/FNG showing peaks corresponding to metallic Ag (blue indices) and hematite $Fe_2O_3$ (red indices). (c) TEM images of Ag/FNG.

The resulting Ag/FNG was identified to form both metallic silver and hematite $Fe_2O_3$ according to the X-ray diffraction (XRD) data (Figure 1b), with the graphene contents of 22.5 wt % according to the thermogravimetric analysis (TGA) results (Figure S1). The TEM images (Figure 1c) show two contrasting particles overlapping over the graphene sheets. The microstructural characterization on Ag/FNG shows the successful creation of a heterojunction interface between metallic Ag and $Fe_2O_3$ (Figure S2). The specific two-step synthesis is necessary to produce the heterojunction, according to the control experiments (see the Supporting Information, Figures S3−S5). The reflux step enables the decoration of the iron oxide particles (as $Fe(OH)_3$) on the graphene, where the exposed Fe−OH moiety becomes a preferential site for the deposition of Ag during the subsequent hydrothermal step, instead of the simultaneous growth of Ag and $Fe_2O_3$ via a one-pot synthesis (see the Supporting Information, Figure S4).

Intrinsic electrochemical properties under dark and laser conditions were measured first using cyclic voltammetry (CV) under static conditions (Figure 2a). Under $O_2$-purged conditions, Ag/FNG shows typical CV curves with hysteresis-loop characteristics and current peak at 0.7 V, where maximized oxygen reduction occurs. By applying 405 nm laser irradiation, both the hysteresis-loop and current peaks disappear, while a nearly reversible sweep of scan directions with a distinct sigmoidal curve shape matches the characteristics of a rotating electrode with a high mass transport. These results suggest laser irradiation on Ag/FNG could create a strong mass transport even in a completely static system. The accelerated mass transport in Ag/FNG is distinct as compared to all the control samples without the heterojunction (Figure S6).

We further conducted EIS to study mass-transport behaviors under dark and laser conditions.[20,21] Under dark conditions at 0.66 V, we applied rotation on Ag/FNG at 1600 rpm as the commonly adopted speed to remove mass-transport limitations toward a full evaluation of catalytic performance.[3,4,14,15,19] The generated Nyquist plots (Figure 2b, rotation conditions) show a significant decrease (91%) of the total resistance with rotation (733.7 Ω, based on a fitting using Figure S7) compared to that without rotation (Figure 2b, static conditions) in the labeled region of low-frequency impedance,[20,22] confirming that this labeled region is responsible for mass-transport change (i.e., lowering of $R_{mt}$). Meanwhile, the points corresponding to charge-transfer resistance ($R_{ct}$) remain nearly identical (Figure 2c). Under laser conditions, the associated $R_{mt}$ was decreased by 59% under static conditions (3350 Ω) and is further lowered to 94% (521.0 Ω) under rotation, without any significant changes in $R_{ct}$.

In addition, the ORR polarization curves under laser (Figure S8) show an increase of current density in the plateau curve region, similar to the scenarios with increased rotation speeds

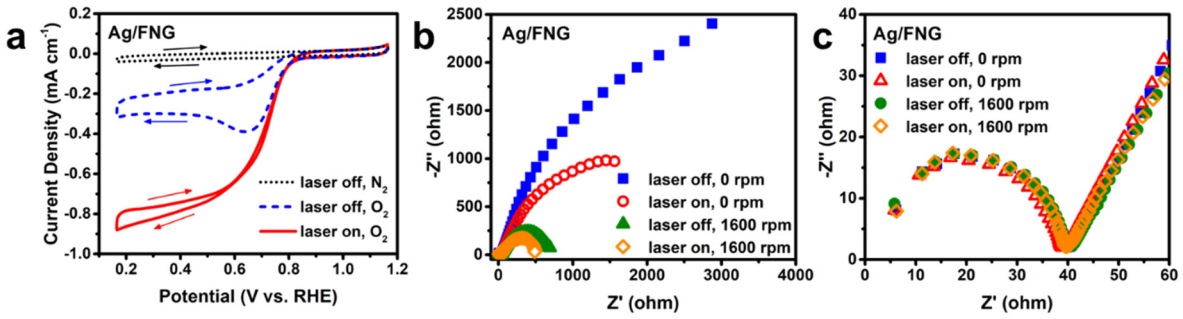


**Figure 2.** Laser-enhanced mass transport in Ag/FNG. (a) CV showing the effects of 405 nm laser in ORR conditions under $O_2$ saturation. (b) EIS Nyquist plots measured under dark/laser and static (0 rpm)/rotation (1600 rpm) conditions at ORR potential (0.66 V). (c) High-frequency region of (b) showing the solution resistance ($R_s$) and the charge-transfer resistance ($R_{ct}$) to be almost equivalent in all measurements. All measurements were done using a rotating disc electrode under $O_2$-saturated 0.1 M KOH.



https://doi.org/10.1021/acs.jpclett.2c00709
J. Phys. Chem. Lett. 2022, 13, 4200−4206

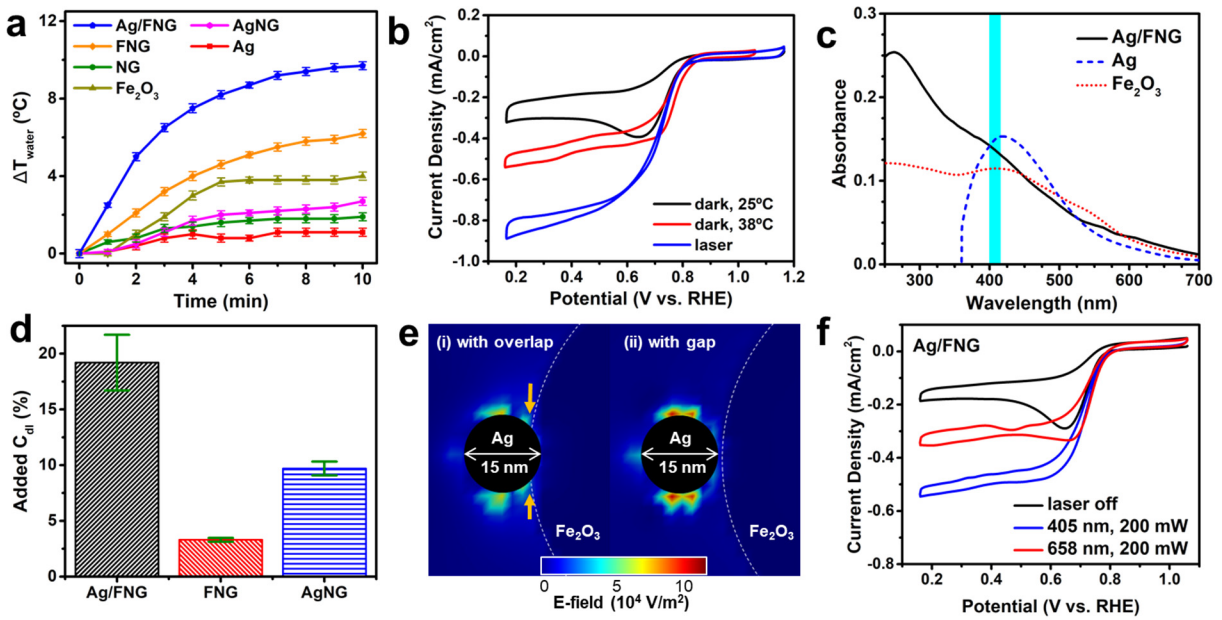


**Figure 3.** Measurements on finding causes of LEMT. (a) Photothermal measurements of catalysts under 400 mW, 405 nm laser (normalized using deionized water as the negative control). (b) CV curves of Ag/FNG under bulk heating with an increase of 13 °C (25−38 °C), in comparison with dark, ambient conditions, and laser conditions. Current density increase under bulk heat is 44% lower than LEMT. (c) UV−Vis absorption spectra of Ag/FNG compared to Ag nanoparticles and hematite $Fe_2O_3$. The light blue band represents the wavelength of the laser used ($\lambda$ = 405 nm). (d) The percentage of the double-layer capacitance ($C_{dl}$) added on Ag/FNG, FNG, and AgNG under laser. (e) Resulting theoretical electric-field map of the interaction between the spherical 15 nm Ag particle (black) and the 75 nm $Fe_2O_3$ particle (white-outlined region to the right of Ag) at 400 mW, 405 nm laser, where (i) a 5 nm overlap and (b) a 1 nm gap was introduced representing heterojunction and heterojunction-free cases, respectively. The orange arrow represents the presence of enhancement at the heterojunction interface. (f) Static CV curves of Ag/FNG under 405 nm laser (blue) and 658 nm laser (red) at the same laser power (200 mW). All CV measurements were done under $O_2$-saturated 0.1 M KOH.

(Figure S9). The insignificant changes of the onset potentials and $R_{ct}$[23] together suggest that the laser irradiation mainly contributes to the mass transport, rather than charge transfer. Thus, laser irradiation acts similar to rotation, which accelerates mass transport.

To study the origin of LEMT at the heterojunction, a series of possible reasons has been proposed, including hot electron, light scattering, photothermal effect, local electromagnetic field enhancement, and dipole−dipole resonance energy transfer.[24] The supposed occurrence of hot electron injection at the heterojunction (from surface plasmonic Ag to semiconductor $Fe_2O_3$),[3,5−9] is unlikely due to the relatively small change among the $R_{ct}$ (Figure 2c).[6] Concerning light scattering, the particle sizes of Ag in Ag/FNG (averaged at ∼17 nm) are smaller than the typical criteria of 50 nm diameter, so the interaction with the laser favors the absorption mechanism (Figure S10).[24,25]

In terms of the photothermal effect (see the experimental setup in the Supporting Information, Figure S11), Ag/FNG can elevate local temperatures by 9.7 °C under laser (Figure 3a), while these of the Ag-free (FNG) and $Fe_2O_3$-free (AgNG) samples are 6.2 and 2.7 °C, respectively. Also, the temperature elevation of graphene-free Ag (1.1 °C) and $Fe_2O_3$ (4.0 °C) are lower than those of AgNG and FNG, respectively, showing the heat-generating contribution of graphene, which probably stems from the nonradiative relaxation of the energy transferred by the laser-absorbing components.[26] The Ag−$Fe_2O_3$ heterojunction, in conjunction with graphene, clearly results in the highest local temperature and, thus, yields the highest mass transport. These results also imply that the combination of plasmonic heating, represented by AgNG, and band gap excitation, represented by FNG, is more effective in accelerating mass transport, rather than just the individual modes.

We also compared the difference between local heat by laser and bulk heat on mass transport evaluated by CV. As shown in Figure 3b, a temperature increase of 13 °C by bulk heating shows a weaker mass transport than the laser condition, which only has a 9.7 °C increase. The local, selective heating by laser is therefore a more convenient way to accelerate mass transport than bulk heating on the entire reactor to increase convection. Yet, these data may also suggest other causes, in addition to local photothermal heating effects, are being involved in the LEMT. We further investigated the effect of local electromagnetic field enhancement at the heterojunction, including near-field enhancement and resonance energy transfer. On the one hand, because resonant energy transfer is characterized as an upconversion excitation,[27] this mechanism is unlikely to occur, since the absorption wavelength of the Ag surface plasmon and the $Fe_2O_3$ band gap is nearly identical (Figure 3c). On the other hand, a near-field enhancement usually requires nearby heterojunction sites to stimulate charge separation under light energy,[17,24] which may refer to an increase of double-layer capacitance ($C_{dl}$) in electrochemical systems (see the Supporting Information, Figure S12).[28] As shown in Figure 3d, the laser irradiation on Ag/FNG raised the $C_{dl}$ by 19.2%, higher than FNG (3.3%) and AgNG (9.7%). These results show that the heterojunction under laser is active toward near-field enhancement. Because of the difficulty of a direct experimental investigation on the heterojunction sites, we further did a theoretical case study.[17,29] (For details, see the Supporting Information, Figure S13.) The presence of a heterojunction by overlapping Ag and $Fe_2O_3$ in the constructed model (Figure 3e-i) leads toward an


https://doi.org/10.1021/acs.jpclett.2c00709
J. Phys. Chem. Lett. 2022, 13, 4200−4206

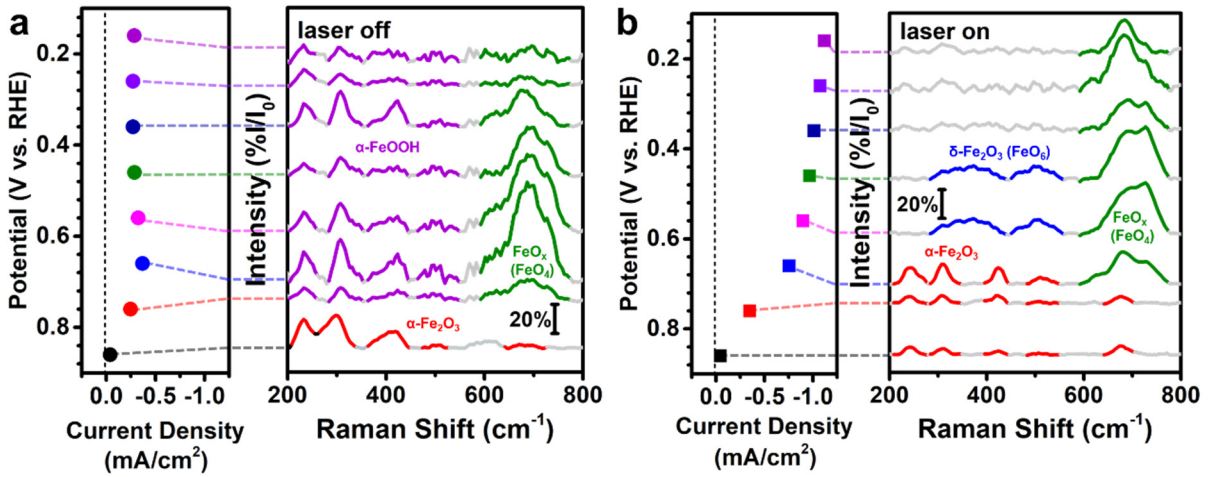


**Figure 4.** Operando Raman spectra under ORR conditions using $O_2$-saturated KOH in the (a) absence and (b) presence of a 405 nm laser. At a certain potential, the left graph shows the corresponding current density with an error of ±0.0047 mA/cm$^2$ (less than 0.5% error in average), while the right shows the associated Raman spectra. All spectra use a 532 nm laser as the Raman light source. All peaks are normalized with the internal standard signal of a graphene D band (Figure S18), whose intensity does not significantly vary during the analysis. On the one hand, the purple signals (307, 432, 372, and 528 cm$^{-1}$) in (a) correspond to $Fe^{III}$−O octahedra ($FeO_6$) in FeOOH, which contains $OH^-$ ligand. On the other hand, the blue signals (350 and 500 cm$^{-1}$) in (b) correspond to $FeO_6$ in hydroxide-free maghemite $Fe_2O_3$.

enhancement of electric fields up to 35 times higher than the heterojunction-free case (Figure 3e-ii). Hence, the near-field enhancement at the heterojunction of Ag/$Fe_2O_3$ was confirmed.

To verify the absorption mechanism is involved in the LEMT, rather than the high-power laser heating up, we changed the laser irradiation wavelength from 405 to 658 nm (Figure 3f). The resulting CV curves are similar to those under dark conditions with no significant mass transport acceleration effect, as compared to that under 405 nm, which is also verified by the results of EIS plots (Figure S14). Since the heating effect by high-powered lasers is not the major origin of mass-transport acceleration, the wavelength-specific absorption at the heterojunction is required to activate LEMT.

Under the same Ag/FNG absorption wavelength, we also measured the LEMT depending on the laser intensity (Figure S15). The resulting CV curves show that the observed plateau curves can be maintained even in small intensities (30 mW), indicating laser absorption, regardless of power, is key toward LEMT. Meanwhile, the current densities of the plateau curves are shown to be directly proportional to the laser intensity with a similar behavior to the effect of rotation speeds (Figure S9). Such dependence of LEMT toward laser intensity enables an intensity-driven control of the mass-transport acceleration, even by just irradiating a selected area.

We attempted to explore the microscopic mechanism of LEMT at the heterojunction through operando Raman spectroscopy under ORR (see the Supporting Information for the setup, Figure S16). At 0.86 V, the Raman data under both dark (Figure 4a) and laser (Figure 4b) conditions show the octahedral $Fe^{III}$−O signals corresponding to hematite $Fe_2O_3$ (red at 298, 414, and 498 cm$^{-1}$).[30,31] By conducting ORR tests, tetrahedral $Fe^{III}$−O signals (green at 691 cm$^{-1}$)[30,32] have appeared, where the trends of the intensity evolution (at 0.76−0.16 V) correspond well to that of the current density, with the peak current and Raman intensity at 0.66 V. These pieces of information suggest $Fe^{III}$−O tetrahedra ($FeO_4$) as the active sites responsible for ORR. Under the laser conditions, similar trends of correlation between current density and presence of tetrahedral $Fe^{III}$−O are shown, yet no $OH^-$ basis species can be detected (see blue parts in Figure 4b identified as maghemite $Fe_2O_3$),[30] opposite to the formation of hydroxide-rich FeOOH[31] under dark (purple parts in Figure 4a). Although the formation of FeOOH from $Fe_2O_3$ under dark ORR conditions has been observed previously,[33] the transformation of hematite to maghemite $Fe_2O_3$ might be the first to be reported on a light-enhanced catalysis. Since $OH^-$ is the main product of ORR electrocatalysis, the selective formation of FeOOH supports an accumulation of hydroxide under dark; hence, the maghemite $Fe_2O_3$ formation can be recognized as the absence of hydroxide under light. Thus, the rapid removal/circulation of hydroxide ions from the electrocatalyst surface to the electrolyte indicates LEMT in the heterojunction.

The operando Raman results also show the presence of superoxide ($O_2^-$) detected at ∼1000 cm$^{-1}$ (cyan) in Figure S17.[34−36] By adding a radical scavenger (*p*-benzoquinone), a decreased ORR current confirms the presence of Fe−$O_2^-$ superoxide moieties observed in the Raman results (Figure S19).[37] The presence of peroxide ($O_2^{2-}$) was also identified at ∼830 cm$^{-1}$ (yellow).[34,38,39] In addition, we observed the negligible changes of peroxide signals in the Raman between dark and laser conditions (Figure S17). Since the charge-transfer pathway should decrease the peroxide quantity,[3] our data reveal the dominant role of the mass-transport route to the charge-transfer pathway.

The band at ∼900 cm$^{-1}$ can be attributed to Ag−OH species (magenta).[36,40,41] Since the results verify the reaction occurs at the heterojunction, we presume that the bound $O_2^{2-}$ should bridge between Ag and Fe and then undergo O−O cleavage, yielding two M−OH bonds as Fe−OH (bond energy 407.0 ± 1.0 kJ/mol) and Ag−OH (bond energy 221 ± 21 kJ/mol).[42] Such a combination is weaker in the total bond energy than two Fe−OH bonds from a pure Fe−O in FNG. However, pure Ag (e.g., only Ag−OH) has a negative impact due to weak oxygen adsorption energy.[14]

All the structural transformations (Figure 4) and adsorbed species (Figure S17) are summarized in Scheme 1 to highlight



https://doi.org/10.1021/acs.jpclett.2c00709
J. Phys. Chem. Lett. 2022, 13, 4200−4206

**Scheme 1. Proposed ORR Mechanisms under Dark and Laser-Enhanced Mass Transport (LEMT) on Ag/FNG[a]**

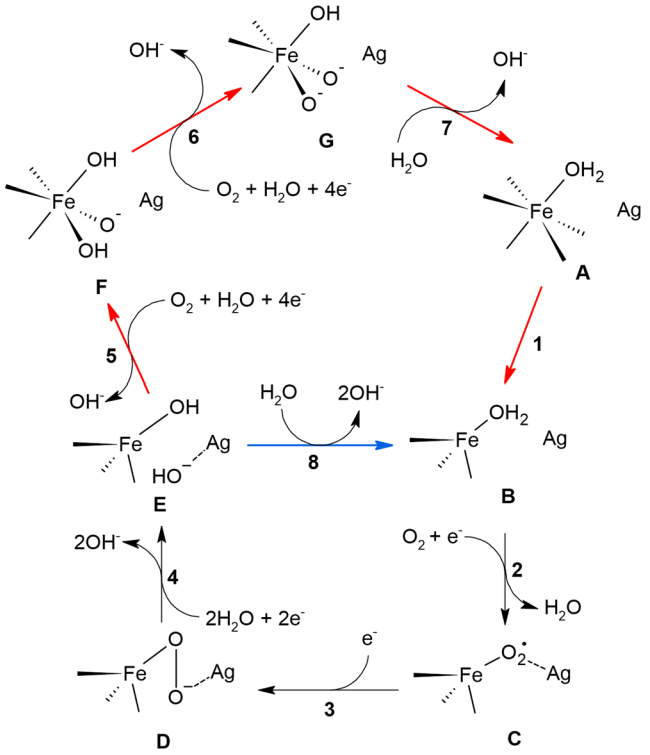


[a]The ORR reaction step starts with the conversion of $FeO_6$ sites to $FeO_4$ (Step 1) at the ORR onset. The $O_2$ molecule adsorbed on the $FeO_4$ sites alongside Ag proceeds to the formation of superoxide-adsorbed complex (Step 2), followed by reduction to peroxide (Step 3) and hydroxide (Step 4) forming Ag−OH and Fe−OH. The dark condition route (Step 5) shows the formation of FeOOH due to the accumulation of adsorbed $OH^-$, taking multiple steps (Steps 6 and 7) to regenerate $FeO_4$. Meanwhile, laser conditions speed up the desorption of hydroxides to regenerate $FeO_4$ (Step 8) due to LEMT.

the LEMT-activated pathway. Since laser irradiation hastens the desorption of $OH^-$ at the Ag/$FeO_4$ heterojunction, this connects to the critical stage of breaking Fe−OH and Ag−OH bonds stimulated by the photothermal effect and near-field enhancement (Scheme 1, Step 8). The photothermal effect should generate local heat to assist hydroxyl bond dissociation. The near-field enhancement polarizes into a negatively charged surface to weaken M−OH bonds and, thus, facilitates the bond dissociation. These two effects should regenerate the active sites of $FeO_4$ from the $FeO_6$ faster than dark conditions, which can be recognized as the additional aspects to understand LEMT.

As indicated above, there are some important unanswered questions regarding the action mechanism of this new ORR catalytic system, such as the quantitative description of laser on the heterojunction, the degrees of charge-transfer contribution to the overall performance, and the influence of laser irradiation on the Gibbs energies of the adsorbed species. An electrokinetic analysis[43] in the absence and presence of a laser could help in determining the enhancement contributions of electronic (charge-transfer-dependent) or concentration (mass-transport-dependent) with regard to the rate-determining step. In situ or operando techniques[44,45] together with synchrotron radiation are helpful to explore the changes in the electronic environment (i.e., oxidation states) by heteroatomic interactions[46] under laser and ORR potential. Undoubtedly, these questions deserve a systematic investigation because they are of great interest to both theoreticians and experimentalists in the field of catalysis to have a more comprehensive understanding of this novel system and to elucidate insights for developing more powerful catalysts.

In this study, we identified that the heterojunction of Ag-iron oxide supported by graphene specifically accelerates mass transport under laser excitation. Both the near-field enhancement and photothermal effects together contribute to LEMT. This new insight would be a useful alternative to understand photon-energy enhanced electrocatalysis. With the suitable heterojunction design, LEMT may become a noncontact, remote-triggering, and high-precision alternative enabling new reaction kinetic studies or device applications that incorporate bulk heating, and matrix turbulence becomes impossible.

## ■ ASSOCIATED CONTENT

### Supporting Information

The Supporting Information is available free of charge at https://pubs.acs.org/doi/10.1021/acs.jpclett.2c00709.

Experimental procedures, high-resolution TEM of Ag/FNG, characterization of heterojunction-free sample, heterojunction intermediate study, characterization of control samples (AgNG, FNG), CV graphs of control samples, corresponding circuit for EIS fitting, ORR LSV curves of Ag/FNG under rotation, particle size survey of Ag in Ag/FNG, photothermal test setup, ECSA changes by LEMT, model image for the theoretical case study, impedance spectra under different laser wavelengths, static CV curves under different laser power, operando Raman setup, operando Raman spectra of the oxygen intermediates and internal standard, and ORR CV graph in the presence of *p*-benzoquinone (PDF)

Transparent Peer Review report available (PDF)

## ■ AUTHOR INFORMATION


### Corresponding Author

**Chun-Hu Chen** − *Department of Chemistry, National Sun Yat-sen University, Kaohsiung 80424, Taiwan;* orcid.org/0000-0002-3512-6880; Email: chunhu.chen@mail.nsysu.edu.tw

### Authors

**Joey Andrew A. Valinton** − *Department of Chemistry, National Sun Yat-sen University, Kaohsiung 80424, Taiwan;* orcid.org/0000-0002-5244-3765

**Min-Chuan Chung** − *Department of Chemistry, National Sun Yat-sen University, Kaohsiung 80424, Taiwan*

Complete contact information is available at: https://pubs.acs.org/10.1021/acs.jpclett.2c00709


### Notes

The authors declare no competing financial interest.

## ■ ACKNOWLEDGMENTS

We acknowledge the financial support from the Ministry of Science and Technology, Taiwan (Project MOST 109-2628-M-110-001-MY3). We thank Prof. C.-L. Lee of National Kaohsiung University of Science and Technology for providing us with Ag nanoparticles and Prof. S.-W. Ding of National Sun Yat-sen University for the help in the theoretical calculations.

Special thanks to Mr. W.-Q. Chen for the help on material synthesis.

## REFERENCES

(1) Huang, Z.-F.; Song, J.; Dou, S.; Li, X.; Wang, J.; Wang, X. Strategies to break the scaling relation toward enhanced oxygen electrocatalysis. *Matter* **2019**, *1* (6), 1494−1518.
(2) Adabi, H.; Shakouri, A.; Ul Hassan, N.; Varcoe, J. R.; Zulevi, B.; Serov, A.; Regalbuto, J. R.; Mustain, W. E. High-performing commercial Fe-N-C cathode electrocatalyst for anion-exchange membrane fuel cells. *Nat. Energy* **2021**, *6* (8), 834−843.
(3) Lin, S.-C.; Hsu, C.-S.; Chiu, S.-Y.; Liao, T.-Y.; Chen, H. M. Edgeless Ag-Pt bimetallic nanocages: in situ monitor plasmon-induced suppression of hydrogen peroxide formation. *J. Am. Chem. Soc.* **2017**, *139* (6), 2224−2233.
(4) Zheng, Z.; Xie, W.; Li, M.; Ng, Y. H.; Wang, D.-W.; Dai, Y.; Huang, B.; Amal, R. Platinum electrocatalysts with plasmonic nanocores for photo-enhanced oxygen-reduction. *Nano Energy* **2017**, *41*, 233−242.
(5) Shi, F.; He, J.; Zhang, B.; Peng, J.; Ma, Y.; Chen, W.; Li, F.; Qin, Y.; Liu, Y.; Shang, W.; Tao, P.; Song, C.; Deng, T.; Qian, X.; Ye, J.; Wu, J. Plasmonic-enhanced oxygen reduction reaction of silver/graphene electrocatalysts. *Nano Lett.* **2019**, *19* (2), 1371−1378.
(6) Liu, G.; Li, P.; Zhao, G.; Wang, X.; Kong, J.; Liu, H.; Zhang, H.; Chang, K.; Meng, X.; Kako, T.; Ye, J. Promoting active species generation by plasmon-induced hot-electron excitation for efficient electrocatalytic oxygen evolution. *J. Am. Chem. Soc.* **2016**, *138* (29), 9128−9136.
(7) He, Q.; Zhou, F.; Zhan, S.; Yang, Y.; Liu, Y.; Tian, Y.; Huang, N. Enhancement of photocatalytic and photoelectrocatalytic activity of Ag modified Mpg-$C_3N_4$ composites. *Appl. Surf. Sci.* **2017**, *391*, 423−431.
(8) Wang, S.-S.; Jiao, L.; Qian, Y.; Hu, W.-C.; Xu, G.-Y.; Wang, C.; Jiang, H.-L. Boosting electrocatalytic hydrogen evolution over metal-organic frameworks by plasmon-induced hot-electron injection. *Angew. Chem., Int. Ed.* **2019**, *58* (31), 10713−10717.
(9) Saada, T. N.; Marques da Silva, A. G.; Subramanian, P.; Pang, L.; Adnane, N.; Djafari-Rouhani, B.; Mishyn, V.; Meziane, D.; Melinte, S.; Sandu, G.; Dumeignil, F.; Paul, S.; Wojcieszak, R.; Boukherroub, R.; Szunerits, S. Plasmon-enhanced electrocatalytic oxygen reduction in alkaline media on gold nanohole electrodes. *J. Mater. Chem. A* **2020**, *8* (20), 10395−10401.
(10) Xiong, Y.; Ren, M.; Li, D.; Lin, B.; Zou, L.; Wang, Y.; Zheng, H.; Zou, Z.; Zhou, Y.; Ding, Y.; Wang, Z.; Dai, L.; Yang, H. Boosting electrocatalytic activities of plasmonic metallic nanostructures by tuning the kinetic pre-exponential factor. *J. Catal.* **2017**, *354*, 160−168.
(11) Zhou, L.; Swearer, D. F.; Zhang, C.; Robatjazi, H.; Zhao, H.; Henderson, L.; Dong, L.; Christopher, P.; Carter, E. A.; Nordlander, P.; Halas, N. J. Quantifying hot carrier and thermal contributions in plasmonic photocatalysis. *Science* **2018**, *362* (6410), 69−72.
(12) Choi, C. H.; Chung, K.; Nguyen, T.-T. H.; Kim, D. H. Plasmon-mediated electrocatalysis for sustainable energy: from electrochemical conversion of different feedstocks to fuel cell reactions. *ACS Energy Lett.* **2018**, *3* (6), 1415−1433.
(13) Liao, P.-C.; Jhang, R.-H.; Chiu, Y.-H.; Valinton, J. A. A.; Yeh, C.-H.; Ebajo, V. D.; Wang, C.-H.; Chen, C.-H. Rock salt oxide hollow spheres achieving durable performance in bifunctional oxygen energy cells. *ACS Appl. Energy Mater.* **2021**, *4* (4), 3448−3459.
(14) Chen, W.-Q.; Chung, M.-C.; Valinton, J. A. A.; Penaloza, D. P.; Chuang, S.-H.; Chen, C.-H. Heterojunctions of silver-iron oxide on graphene for laser-coupled oxygen reduction reactions. *Chem. Commun. (Cambridge, U. K.)* **2018**, *54* (57), 7900−7903.
(15) Ashok, A.; Kumar, A.; Matin, M. A.; Tarlochan, F. Synthesis of highly efficient bifunctional Ag/$Co_3O_4$ catalyst for oxygen reduction and oxygen evolution reactions in alkaline medium. *ACS Omega* **2018**, *3* (7), 7745−7756.
(16) Guo, L.; Liang, K.; Marcus, K.; Li, Z.; Zhou, L.; Mani, P. D.; Chen, H.; Shen, C.; Dong, Y.; Zhai, L.; Coffey, K. R.; Orlovskaya, N.; Sohn, Y.-H.; Yang, Y. Enhanced photoelectrocatalytic reduction of oxygen using Au@$TiO_2$ plasmonic film. *ACS Appl. Mater. Interfaces* **2016**, *8* (51), 34970−34977.
(17) Seh, Z. W.; Liu, S.; Low, M.; Zhang, S.-Y.; Liu, Z.; Mlayah, A.; Han, M.-Y. Janus Au-$TiO_2$ Photocatalysts with strong localization of plasmonic near-fields for efficient visible-light hydrogen generation. *Adv. Mater.* **2012**, *24* (17), 2310−2314.
(18) Liu, Z.; Jiang, D.; Yang, L.; Yu, J.; Li, X.; Liu, X.; Zhao, L.; Zhang, X. L.; Han, F.; Zhou, W.; Liu, H. Plasmon-enhanced hydrogen evolution reaction kinetics through the strong coupling of Au-O Bond on Au-$MoO_2$ heterostructure nanosheets. *Nano Energy* **2021**, *88*, 106302.
(19) Kao, W.-Y.; Chen, W.-Q.; Chiu, Y.-H.; Ho, Y.-H.; Chen, C.-H. General solvent-dependent strategy toward enhanced oxygen reduction reaction in graphene/metal oxide nanohybrids: effects of nitrogen-containing solvent. *Sci. Rep.* **2016**, *6*, 37174.
(20) Singh, R. K.; Devivaraprasad, R.; Kar, T.; Chakraborty, A.; Neergat, M. Electrochemical impedance spectroscopy of oxygen reduction reaction (ORR) in a rotating disk electrode configuration: effect of ionomer content and carbon-support. *J. Electrochem. Soc.* **2015**, *162* (6), F489−F498.
(21) Zhu, W.; Pei, Y.; Liu, Y.; Zhang, J.; Qin, Y.; Yin, Y.; Guiver, M. D. Mass transfer in a Co/N/C catalyst layer for the anion exchange membrane fuel cell. *ACS Appl. Mater. Interfaces* **2020**, *12* (29), 32842−32850.
(22) Joshi, P.; Okada, T.; Miyabayashi, K.; Miyake, M. Evaluation of alkylamine modified Pt nanoparticles as oxygen reduction reaction electrocatalyst for fuel cells via electrochemical impedance spectroscopy. *Anal. Chem.* **2018**, *90* (10), 6116−6123.
(23) Bard, A. J.; Faulkner, L. R. *Electrochemical Methods: Fundamentals and Applications,* 2nd ed.; Wiley Textbooks: New York, 2000.
(24) Zhang, N.; Han, C.; Fu, X.; Xu, Y.-J. Function-oriented engineering of metal-based nanohybrids for photoredox catalysis: exerting plasmonic effect and beyond. *Chem.* **2018**, *4* (8), 1832−1861.
(25) Ingram, D. B.; Linic, S. Water splitting on composite plasmonic-metal/semiconductor photoelectrodes: evidence for selective plasmon-induced formation of charge carriers near the semiconductor surface. *J. Am. Chem. Soc.* **2011**, *133* (14), 5202−5205.
(26) Zhang, Y.; Gurzadyan, G. G.; Lu, R.; Zhang, S.; Jin, X.; Tang, B. Efficient photothermal conversion of $Fe_2O_3$-RGO guided from ultrafast quenching effect of photoexcited state. *AIChE J.* **2020**, *66* (6), No. e16975.
(27) Cushing, S. K.; Li, J.; Meng, F.; Senty, T. R.; Suri, S.; Zhi, M.; Li, M.; Bristow, A. D.; Wu, N. Photocatalytic activity enhanced by plasmonic resonant energy transfer from metal to semiconductor. *J. Am. Chem. Soc.* **2012**, *134* (36), 15033−15041.
(28) Hoener, B. S.; Zhang, H.; Heiderscheit, T. S.; Kirchner, S. R.; De Silva Indrasekara, A. S.; Baiyasi, R.; Cai, Y.; Nordlander, P.; Link, S.; Landes, C. F.; Chang, W.-S. Spectral response of plasmonic gold nanoparticles to capacitive charging: Morphology Effects. *J. Phys. Chem. Lett.* **2017**, *8* (12), 2681−2688.
(29) Thomann, I.; Pinaud, B. A.; Chen, Z.; Clemens, B. M.; Jaramillo, T. F.; Brongersma, M. L. Plasmon enhanced solar-to-fuel energy conversion. *Nano Lett.* **2011**, *11* (8), 3440−3446.
(30) Chamritski, I.; Burns, G. Infrared- and raman-active phonons of magnetite, maghemite, and hematite: a computer simulation and spectroscopic study. *J. Phys. Chem. B* **2005**, *109* (11), 4965−4968.
(31) de Faria, D. L. A.; Venâncio Silva, S.; de Oliveira, M. T. Raman microspectroscopy of some iron oxides and oxyhydroxides. *J. Raman Spectrosc.* **1997**, *28* (11), 873−878.
(32) Jubb, A. M.; Allen, H. C. Vibrational spectroscopic characterization of hematite, maghemite, and magnetite thin films produced by vapor deposition. *ACS Appl. Mater. Interfaces* **2010**, *2* (10), 2804−2812.
(33) Chen, H.; Song, T.; Lin, L.; Qin, H.; He, Y.; Huang, Y.; Ni, H.; He, J.; Zhang, J.; Zhang, W. Unraveling the valence state and phase


https://doi.org/10.1021/acs.jpclett.2c00709
J. Phys. Chem. Lett. 2022, 13, 4200−4206

transformation of iron-based electrocatalysts towards oxygen reduction reaction. *J. Alloys. Compd.* **2021**, *877*, 160274.
(34) McBreen, P. H.; Moskovits, M. A surface-enhanced Raman study of ethylene and oxygen interacting with supported silver catalysts. *J. Catal.* **1987**, *103* (1), 188−199.
(35) Krupenie, P. H. The spectrum of molecular oxygen. *J. Phys. Chem. Ref. Data* **1972**, *1* (2), 423−534.
(36) Wang, C.-B.; Deo, G.; Wachs, I. E. Interaction of polycrystalline silver with oxygen, water, carbon dioxide, ethylene, and methanol: in situ Raman and catalytic studies. *J. Phys. Chem. B* **1999**, *103* (27), 5645−5656.
(37) Ding, X.; Zhao, K.; Zhang, L. Enhanced photocatalytic removal of sodium pentachlorophenate with self-doped $Bi_2WO_6$ under visible light by generating more superoxide ions. *Environ. Sci. Technol.* **2014**, *48* (10), 5823−5831.
(38) Ho, R. Y. N.; Que, L., Jr.; Roelfes, G.; Feringa, B. L.; Hermant, R.; Hage, R. Resonance Raman evidence for the interconversion between an $[Fe^{III}\text{-}\eta^1\text{-}OOH]^{2+}$ and $[Fe^{III}\text{-}\eta^2\text{-}O_2]^{+}$ species and mechanistic implications thereof. *Chem. Commun. (Cambridge, U. K.)* **1999**, No. 21, 2161−2162.
(39) Hester, R. E.; Nour, E. M. Resonance Raman studies of transition metal peroxo complexes: 2-The purple intermediate formed in the reactions of iron(II) and iron (III)ethylenediaminetetraacetate with superoxide and hydrogen peroxide, respectively. *J. Raman Spectrosc.* **1981**, *11* (1), 35−38.
(40) Itoh, T.; Sasaki, Y.; Maeda, T.; Horie, C. In situ SERS study of water molecules on silver electrodes in alkali-hydroxide solutions. *Surf. Sci.* **1997**, *389* (1), 212−222.
(41) Bao, X.; Muhler, M.; Pettinger, B.; Uchida, Y.; Lehmpfuhl, G.; Schlögl, R.; Ertl, G. The effect of water on the formation of strongly bound oxygen on silver surfaces. *Catal. Lett.* **1995**, *32* (1), 171−183.
(42) Luo, Y. R. *Comprehensive Handbook of Chemical Bond Energies;* CRC Press: Boca Raton, FL, 2007.
(43) Bai, L.; Hsu, C.-H.; Alexander, D. T. L.; Chen, H. M.; Hu, X. Double-atom catalysts as a molecular platform for heterogeneous oxygen evolution electrocatalysis. *Nat. Energy* **2021**, *6*, 1054−1066.
(44) Zhu, Y.; Kuo, T.-R.; Li, Y.-H.; Qi, M.-Y.; Chen, G.; Wang, J.; Xu, Y.-J.; Chen, H. M. Emerging dynamic structure of electrocatalysts unveiled by *in situ* X-ray diffraction/absorption spectroscopy. *Energy Environ. Sci.* **2021**, *14* (4), 1928−1958.
(45) Zhu, Y.; Wang, J.; Chu, H.; Chu, Y.-C.; Chen, H. M. *In situ/operando* studies for designing next-generation electrocatalysts. *ACS Energy Lett.* **2020**, *5* (4), 1281−1291.
(46) Sun, H.; Tung, C.-H.; Qiu, Y.; Zhang, W.; Wang, Q.; Li, Z.; Tang, J.; Chen, H.-C.; Wang, C.; Chen, H. M. Atomic metal-support interaction enables reconstruction-free dual-site electrocatalyst. *J. Am. Chem. Soc.* **2022**, *144* (3), 1174−1186.





https://doi.org/10.1021/acs.jpclett.2c00709
*J. Phys. Chem. Lett.* 2022, 13, 4200−4206